The effects of 4% barium doping on the morphological, strutural and dielectric characteristics of $(Na_{0.5}Bi_{0.5})[(Ti_{0.8}Zr_{0.2})_{0.9}(Nb_{2/3}Zn_{1/3})_{0.1}]O_3$

S. Bouali[a], K. Bounab[b,*], H. Menasra[b], Z. Necira[b], M. Abba[c]
[a]*Laboratory of Materials Chemistry and the living:Activity&Reactivity (LCMVAR), Faculty of Matter Sciences, Departement of chemistry, University of Batna 1, 05000, Batna, Algeria*
[b]*Laboratory of Applied Chemistry, Departement of Science of Matter, University of Biskra, BP 145 RP, Biskra 07000, Algeria*
[c]*Laboratory of Molecular Chemistry and Environment, University of Biskra, Algeria BP 145 RP, Biskra 07000, Algeria*

In this study, perovskite ceramics $(Na_{0.5}Bi_{0.5})_{1-x}Ba_x[(Ti_{0.8}Zr_{0.2})_{0.9}(Nb_{2/3}Zn_{1/3})_{0.1}]O_3$ ($NB_{1-x}B_xTZNZ$) were prepared using the molten salt method. The sintering process was conducted at 1100°C for 4 hours in an air atmosphere. The crystal structure was examined using X-ray powder diffraction, which indicated that the material crystallized in a tetragonal structure with a space groupe P4bm. However, there was also evidence of 6% pyrochlore phase present. The crystallite size was found to decrease with Barium doping, and this decrease was attributed to the pinning effect of grain boundaries resulting from the formation of oxygen vacancies which reduce the AC conductivity values. Scanning electron microscopy was employed to examine the grain morphologies, revealing that the sample exhibited a compact structure. Additionally, the density of ($NB_{1-x}B_xTZNZ$) (x=0.04) was observed to be higher compared to ($NB_{1-x}B_xTZNZ$) (x=0.00). Barium doped into $NB_{1-x}B_xTZNZ$ also caused a decrease in dielectric constant and dielectric loss. Raman spectroscopy was performed at room temperature on the doped ceramic with Barium, and we discussed the incorporation of Ba^{2+} in A-site of the perovskite ABO_3.

(Received August 2, 2023; Accepted November 16, 2023)

Keywords: BNT, Molten salt, Perovskite, Tetragonal, Dielectric properties

1. Introduction

Perovskites structures encompass a wide range of materials with the general formula ABO_3. These materials have been extensively studied due to their structural versatility and desirable properties, such as $La_{1-x}B_{2+x}MnO_3$ (magnetic) $KNbO_3$ (ferroelectric), $PbZr_{1-x}Ti_xO_3$ (piezoelectric)[1,2]. Lead-based materials including $PbTiO_3$(ferroelectric) and $PbZrO_3$(antiferroelectric), have received considerable attention and found successful applications [1,3].However, the toxicity and high vapor pressure of Lead (Pb) oxide during processing has led researchers to explore environmentally friendly and biocompatible alternatives to lead-based piezoelectric ceramics [4,5].

$Bi_{0.5}Na_{0.5}TiO_3$ (BNT) have emerged as promising candidates due to their environmental friendliness and excellent ferroelectric and piezoelectric properties [6]. Sodium bismuth titanate (BNT) was first studied by Smolenk et al and it has been extensively studied by various researchers [7, 8, 9], and is known for its ABO_3 perovskite structure with complex Bi^{3+} and Na^+ occupancy at the A-site [10].The lone pair effect of Bi^{3+}ion, which is responsible for high polarization, is similar to that of Pb^{2+} [11,12].

Doping at the A-site and B-site and simultaneous substitution have proven effective in improving the properties of BNT- based ceramics [13,14]. Moreover, A-site modification has shown greater effectiveness for BNT-based ceramics compared to B-site modifications [11]. Also,

*Corresponding author : karima.bounab@univ-biskra.dz
https://doi.org/10.15251/DJNB.2023.184.1409

The addition of Ba^{2+} ions affects the composition and electrical characteristics of BNT based ceramics [15,11].

The molten salt method, known for its thermal stability and high thermal and electrical conductivity, has diverse applications. In this method, molten salts such as NaCl and KCl are used to facilitate ion diffusion [16]. These salts enable the production of homogeneous and ultrafine powders [17].And this article highlights the fruitful molten salt in the preparation of perovskite with general formula ABO_3.

Lead-free piezoelectric materials doped with Barium have been studied as excellent candidates for reducing environmental damage. The sodium and bismuth titanate families that fall under perovskite-type ceramics are seen as suitable for carrier and high-energy applications with high Curie temperature. NBBT compounds exhibit good stability properties, so they are excellent candidates for piezoelectric sensors as replacements for lead-based systems, the $(Bi_{0.5}Na_{0.5})TiO_3$-$BaTiO_3$ (BNT-BT) is found by Takenaka et al [18]. It has been one of he most important lead-free ceramics due to its excellent piezoelectric properties around MPB where x=0.06-0.07. However, a recent study of BNT-BT systems indicates that a new phase exists with a composition range between x=0.06 and x=0.10 which is defined as a relaxor ferrielectric phase [19].

The dielectric properties for (1-x)BNT-xBT with the composition of x=0.06, 0.07 and 0.11 are investigated. Compared to conventional relaxing ferroelectrics, the dielectric permittivity as a function of the temperature of BNT-BT composition with $x \leq 0.06$ and $x \geq 0.11$ exhibit a large increase in ε_r at the depolarization temperature, Td, where a ferroelectric at a ferrielectric transition takes place [18].

In this study, we have chosen to substitute Bi^{3+} and Na^{+} ions with Ba^{2+} ions in $(Na_{0.5}\ Bi_{0.5})[(Ti_{0.8}\ Zr_{0.2})_{0.9}\ (Nb_{2/3}Zn_{1/3})_{0.1}]O_3$ or $NB_{1-x}B_xTZNZ(x=0)$ ceramic, resulting in the formation $(Na_{0.5}\ Bi_{0.5})_{0.96}\ Ba_{0.04}[(Ti_{0.8}\ Zr_{0.2})_{0.9}\ (Nb_{2/3}\ Zn_{1/3})_{0.1}]O_3$ or $NB_{1-x}B_xTZNZ(x=0.04)$.

This work aims to investigate the structural, morphological, and dielectric characteristics of $NB_{1-x}B_xTZNZ$ (x=0.04).

2. Experimental procedure

2.1. Samples preparation

The ceramics $(Na_{0.5}\ Bi_{0.5})[(Ti_{0.8}\ Zr_{0.2})_{0.9}(Nb_{2/3}Zn_{1/3})_{0.1}]O_3$ and $(Na_{0.5}Bi_{0.5})_{0.96}Ba_{0.04}[(Ti_{0.8}\ Zr_{0.2})_{0.9}\ (Nb_{2/3}Zn_{1/3})_{0.1}]O_3$ were prepared using the Molten Salt Method (MSM). The starting oxide powders presented in table 1 were mixed with the salt (NaCl,KCl) in 1:1 ratio. The mixture was crushed in a glass mortar for 6 hours, and then the obtained mixture was calcined at 900°C. To remove the existing salt, the calcined material was repeatedly washed with hot water until no chloride ions were detected, confirmed by testing with $AgNO_3$ solution. The resulting powder was dried at 100°C and crushed for 6 hours to regrind and reduce agglomerates formed during the calcinations process.

The sintering step is crucial in ceramic production. Pellets were formed by pressing the powder. The most important phase in the production of the ceramic is the sintering step at different temperatures (1050°C, 1100°C, 1150°C, and 1200°C). The schematic diagram of synthesis procedure is illustrated step-by step in figure1.

Table 1. The commercial precursors used and their properties.

Trade Name	Precursors	Molar Mass(g/mol)	Purity
Barium carbonates	$BaCO_3$	197.34	99%
Bismuth oxide	Bi_2O_3	465.95	99
Sodium carbonate	Na_2CO_3	105.99	99.5
Titanium dioxide	TiO_2	79.865	99
Zirconium dioxide	ZrO_2	123.222	99
Niobium pentoxide	Nb_2O_5	265.8090	99.99
Zinc oxide	ZnO	81.3800	99.5

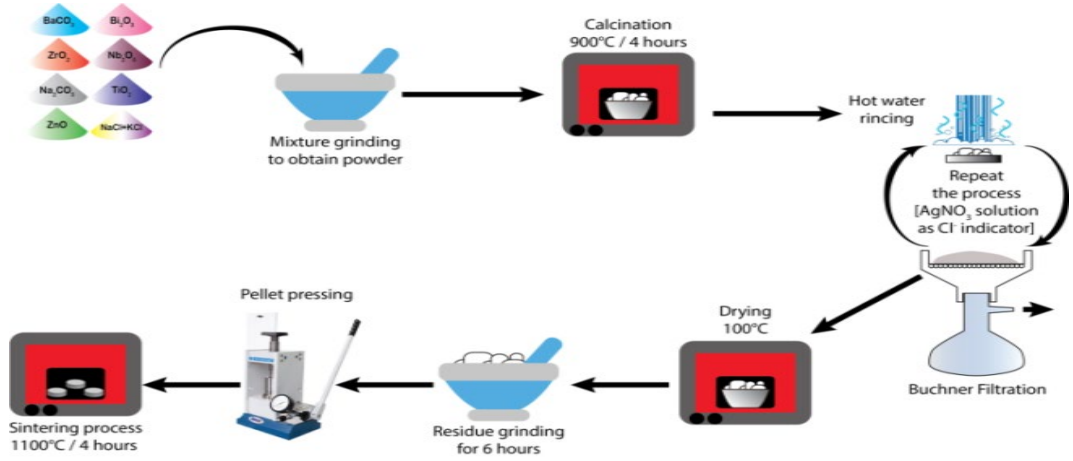

Fig. 1. The synthesis process of $(Na_{0.5}\ Bi_{0.5})_{1-x}Ba_x[(Ti_{0.8}\ Zr_{0.2})_{0.9}(Nb_{2/3}\ Zn_{1/3})_{0.1}]O_3$ceramics by Molten-salt method.

2.2. Samples characterization

For structural characterization purpose (XRD) as prepared ceramics, the pellets were first crushed into fine powders.Then the structural phases were studied at room temperature by X-ray diffraction (XRD) using a vertical diffractometer " BRUKER-AXE type D8" advance with CuKα radiation(λ= 1.5406Å), All diffraction diagrams are recorded in the angular domain $10°<2\theta<70°$, which may be sufficient for the identification of the different phases. We note that we used X'pert HighScore for analyzing and indexing the different lines.The pellet density is calculated using Archimedes' method.

The Raman spectra of sintered ceramics were analyzed using a micro-Raman spectrometer (LABRAM HRT 4600 HR 800, LaMMA, Sfax,Tunisia) with a laser excitation line of 633 nm in the frequency range 50-1000cm^{-1}. The microstructures of the samples were analyzed by Scanning electron microscopy (SEM) (JEOL JSM-63901v). An operating system allows a computer to regulate it. The goal of these micrographs is to study the morphology of our samples.

The dielectric loss (tanδ), and relative dielectric permittivity (ε_r) measurements were carried out using an impedance meter HP4284A.

3. Results and discussion

3.1. Density

The study of density is important in optimizing the sintering temperature, as higher density indicates better material quality [20]. For the composition $NB_{1-x}B_xTZNZ$ (x=0 and x=0.04) at various sintering temperatures from 1050°C to 1200°C were tested to achieve the densest ceramic. The densities diagram in figure 2 shows the relationship between density and temperature.

Density initially increased with the sintering temperature until reached the optimum density, after which it decreased. However, a significant change in density was observed for the ceramic doped with Barium. Both compositions generally showed the same trend, with density increasing with the sintering temperature and reaching a maximum value of 5.87g/cm^3 at 1100°C for $NB_{1-x}B_xTZNZ$ (x=0.04). Therefore, the optimum sintering temperature was determined to be 1100°C.

The increase in density indicates a compact structure with fewer pores [9,21]. To determine the experimental density, the following formula was used [22], is presented in table 2.

$$\rho_{exp}=\frac{m}{\pi\times t\times r^2} \quad (1)$$

Here, m, t and r represent the masse, thickness, and radius of the prepared pellet samples, respectively. We chose the composition at the optimal temperature for the rest of our study.

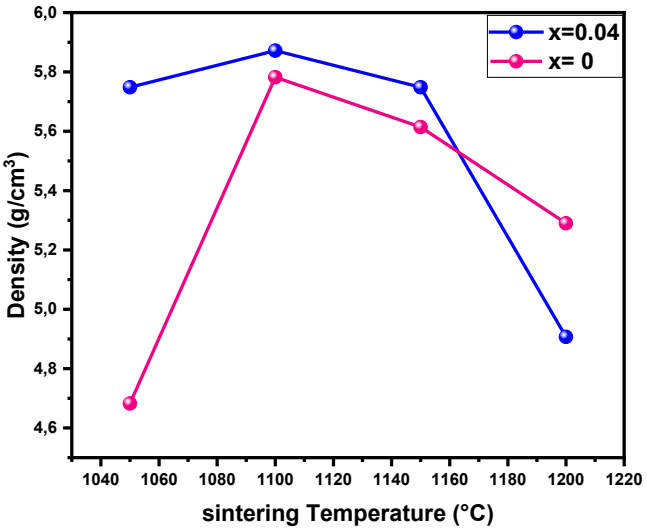

Fig. 2. Illustrates the evolution of density as a function of the sintering temperature for $NB_{1-x}B_xTZNZ$ (x=0 and x=0.04) ceramics.

3.2. XRD

Moving on to the X-ray diffraction XRD analysis, figure 3a shows the XRD pattern of the $NB_{1-x}B_xTZNZ$ (x=0 and x=0.04) ceramics sintered at 1100°C for 4 hours. It indicates the formation of a perovskite structure. Based on tetragonal symmetry, with space group P4bm the XRD pattern was indexed. We used X'Pert HighScore for analyzing and indexing the different lines. The average diffraction peaks matched with ICSD card N° 98-028-0984. There was a good agreement between the X-ray peak position and the reference pattern. However, a small amount (6%) of the pyrochlore phase was present.

When comparing the XRD pattern of the undoped ceramic with the pattern of the barium doped ceramic, the diffraction peaks (002) and (220) shifted significantly toward lower angles due to the different lattice parameter of samples [15], the magnified image of this diffraction peaks is shown in figure 3b.The size of Ba^{2+} (0.161 nm) with a coordination number of 12 is bigger than

the average radius of ($Bi^{3+}$and Na^{+}) leading to increased lattice constant, and cell volume which are indicated in table 2. and downward shift of the peak positions [23,11].

The substitution of Ba^{2+} for A site ions usually causes an increase in lattice parameter and interplanar spacing according to the formula for Bragg diffraction[24, 28] :

$$2d\sin\theta = n\lambda \quad (2)$$

where d is the interplanar spacing, θ is the diffraction angle. The increase in the cell parameter confirms the perfect incorporation of Ba^{2+} ion into the $NB_{1-x}B_xTZNZ$(x=0) lattice [11]. Goldschmidt tolerance factor (t) is generally used to determine the stability of a perovskite structure, and the degree of lattice distortion associated with it [11,25, 20]

The formula for the tolerance factor is:

$$t = \frac{r_A + r_o}{\sqrt{2} + (r_B + r_o)} \quad (3)$$

where r_A: average ionic radius of A-site atoms, r_B: average ionic radius of B-site atoms. And r_O : the ionic radius of the O^{-2} ion.

The tolerance factor for $NB_{1-x}B_xTZNZ$ (x=0) compound is calculated to be: 0.9268 using the above equation, and the value of t=0.9314 for $NB_{1-x}B_xTZNZ$ (x=0.04) is attributed to be slightly increased after adding Ba^{2+} [11], with : R(O)=1.40Å, R(Ba^{2+})=1.61Å, R(Na^{+})=1.39Å, R(Bi^{3+})=1.17Å, R(Zr^{4+})= 0.72Å, R(Ti^{4+})= 0.60Å, R(Zn^{2+})=0.9Å and R(Nb^{5+})=0.74Å.

The decrease in lattice strain from 0.081% to 0.027% implies a decrease in the distortion of the crystal structure. therfore, decreasing the lattice strain by changing the composition in the perovskite system can increase the tolerance factor. The lattice strain was calculated from the following equation [25]:

$$\frac{\Delta L}{L} = \frac{Lc - La}{Lc} \times 100 \quad (4)$$

where La is the a lattice parameter of $NB_{1-x}B_xTZNZ$ (x=0 and x=0.04) ceramics, and Lc is the reference lattice parameter of the tetragonal structure P4bm (ICSD card N° 98-028-0984).

With the addition of Ba^{2+} the peak positions shift towards lower angle and the peak is also getting broadened it implies that crystallite size was decreasing with addition of Barium [26], this is confirmed after calculating the crystallite size with two methods, Deby-scherre and Williamson-Hall method. In addition, we have collected these values in table 2. The change of lattice parameter value indicates the interrogation of the Ba^{2+}dopant in A-site [22].

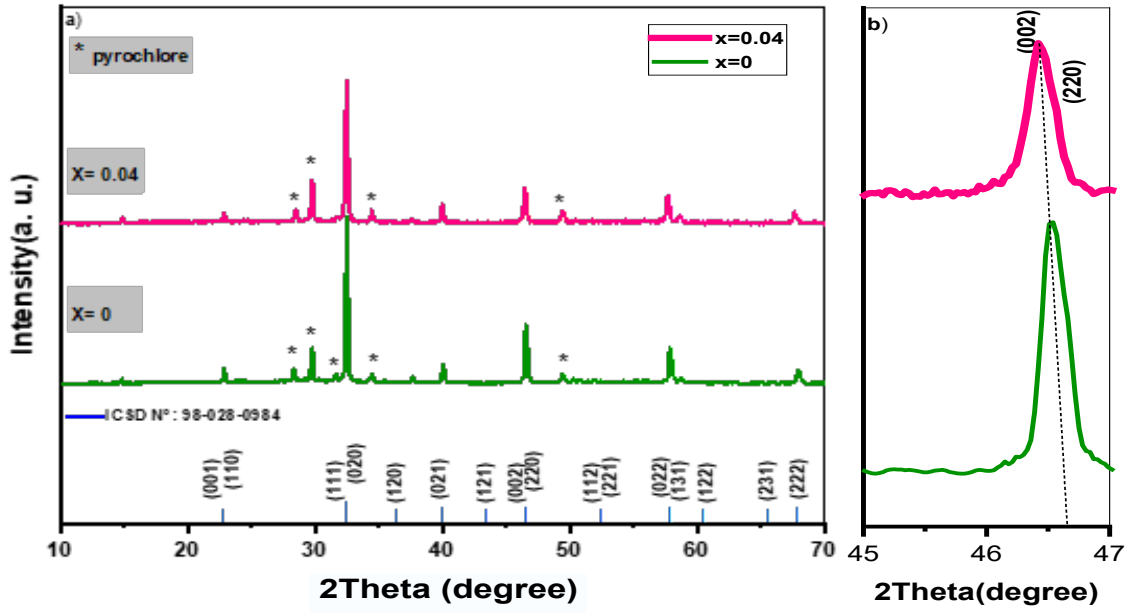

Fig. 3. a) X-ray indexed diffraction patterns of $NB_{1-x}B_xTZNZ$ (x=0 and x=0.04) ceramics. b) XRD in the range of 2θ [45°-47°].

We calculated the Lattice parameters with two methods: Using (hkl) values and inter planar spacing [22] and by using the Cellref program [27].

Using (hkl) values and interplanar spacing according to the relation, the lattice parameters of the tetragonal structure were determined:

$$\frac{1}{d^2} = \frac{h^2+k^2}{a^2} + \frac{l^2}{c^2} \tag{5}$$

The lattice parameters were calculated from the XRD data using the two methods as shown in table 2, also, the volume of the Unit cell of the synthesized samples have determined by multiplying a^2*c and presented in table 2. [22].

The X-ray density of the synthesized sample have determined by equation [22].

$$\rho_{Cal} = {}^{Z\,M}/_{V_a\,N} \tag{6}$$

where Z, M, Na and V is the number atoms per unit cell, the molar masse, Avogadro's number and lattice constant of samples respectively.

The following relation was used to determine the porosity of $NB_{1-x}B_xTZNZ$ samples :

$$p = \left(1 - \frac{\rho_{exp}}{\rho_{Cal}}\right) \times 100 \tag{7}$$

Table 2. Structural parameters of $NB_{1-x}B_xTZNZ$(x=0 and x=0.04).

Samples	Lattice parameters Calculated (Å)		Lattice parameters obtained by Cellref (Å)		cell volume (Å^3)	Density (g/cm^3)		Grain size (µm)	Average crystallite size (nm)		Porosity %
	a=b	c	a=b	c	V	ρ_{exp}	ρ_{cal}		Deby-Scherrer	Williamson-Hall	
x=0	5.513	3.893	5.5135	3.9103	118.87	5.78	6.63	2.249	43.4351	48.31	0.13
x=0.04	5.526	3.892	5.5165	3.9098	118.98	5.87	6.66	2.010	36.086	45.76	0.12

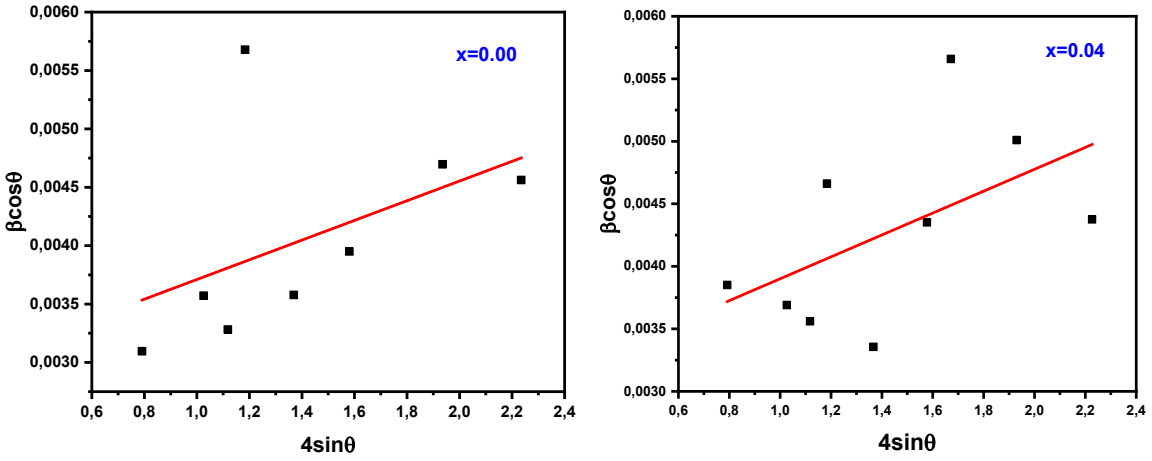

Fig.4. Williamson-Hall (W-H) analysis of $NB_{1-x}B_xTZNZ$ (x=0 and x=0.04) Sintered at 1100°C.

Crystallite size D was estimated using Deby Scherrer's equation Dsch and Williamson-Hall method Dw-h as follows [29,22,30]:

$$D_{Sch} = \frac{K\lambda}{\beta \cos\theta} \tag{8}$$

and

$$\beta \cos\theta = \frac{K\lambda}{D_{W-H}} + 4\varepsilon \sin\theta \tag{9}$$

where K= 0.9 is the Scherrer constant, D is the crystallite size, λ = 0.154 nm is the wave-length of the x-ray source, ε is the strain and θ is the diffraction angle corresponds to the radian peak position.

The fitting line obtained when plotting βcosθ versus 4sinθ is used to estimate the average crystallite size, D [31].

Figure.4 shows the Williamson Hall plot approach, the slope of the plot βcosθ versus 4sinθ gives the value of microstrain and intercept results crystallite size.

It is evident from the table.2 that the crystallite size DW-H for the composition $NB_{1-x}B_xTZNZ$ (x=0) achieves a maximum value of 48.311nm and that after adding Ba^{2+}, the crystallite size dropped to 45.76nm. Same thing for the Deby-Scherrer method the crystallite size decreases from 43.4351nm to 36.086nm.

In the Williamson-Hall method, the broadening due to strain is completely suppressed and thus the crystallite size is larger when compared to the deby-scherrer method [32].

3.3. RAMAN spectroscopy

The ceramics samples were also investigated by Raman spectroscopy.This technique is used to analyze the structure and phase shift of $NB_{1-x}B_xTZNZ$ ceramics and examine vibration, rotational and other low frequency modes [22]. Figure 5 represents the Raman scattering spectra of $NB_{1-x}B_xTZNZ$ (x=0, x=0.04) were performed in the range 100 to 1000 cm^{-1} at room temperature.

According to figure 5 compared to that of undoped ceramic the Raman modes for $NB_{1-x}B_xTZNZ$ (x=0.04) are much stronger, suggesting that the crystallinity of the undoped ceramic is enhanced by the addition of Ba^{2+} ions [22,15].

About four regions were detected in the spectra and they are almost identical to those previously reported for BNT based ceramics [33, 9,24]. This ceramic sample can be deconvolated into five main peaks which are located at: 110, 264, 531, 624 et 800 cm^{-1} which agrees with the reports of other researchers [6,8].

The peak at 110cm^{-1} is mainly affected by the Na^{+}, Bi^{3+} and Ba^{2+} of the A-site vibration in the ABO_3 style perovskite ceramics [33,34,24]. This wavennumber confirms the presence of a larger volume of Ba^{2+} in the $NB_{1-x}B_xTZNZ$(x=0.04) compared with (Na^{+}, Bi^{3+}) [35].

200-450 cm-1 modes could be related to the vibration of Ti-O [6]. Also, the peaks in the range from 450 to 700 cm^{-1} are associated with the TiO_6 octahedra vibration,and the high frequency regions above 700cm^{-1} were seen to be related to A_1(longitudinal optical) and E (longitudinal optical) overlapping bands [33,6].

The Raman spectroscopy results confirm that the formation of the perovskite structure was successful, which is confirmed by XRD.

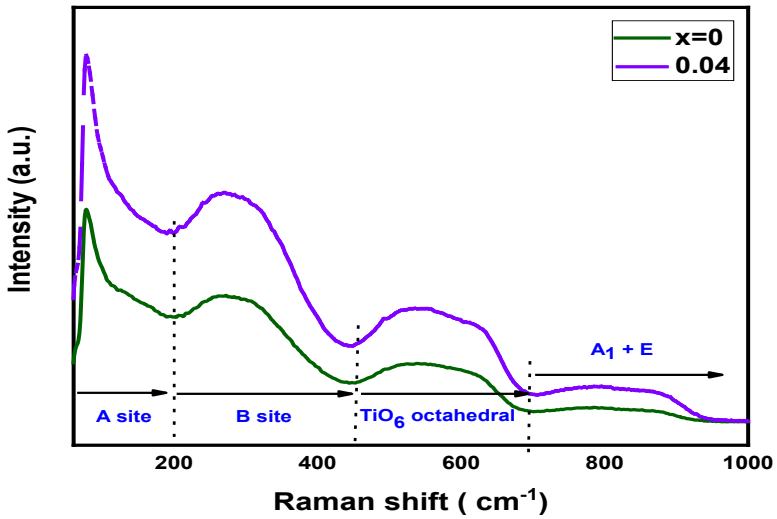

Fig. 5. Raman spectrum of $NB_{1-x}B_xTZNZ$ (x=0 and x= 0.04) at room temperature.

3.4. SEM micrographe

Scanning electron microscopy images of surfaces and grains size distribution of $NB_{1-x}B_xTZNZ$ (x=0 and x=0.04) samples are shown in figure 6. The histograms of average grains size were calculated using Image j software. The data obtained were adjusted utilizing the 'Gaussian function' as demonstrated in figure 6.

Through it, we can say that the ceramic $NB_{1-x}B_xTZNZ$ (x=0.04) is dense and the porosity is low. After adding Barium, the average grain size of $NB_{1-x}B_xTZNZ$ (x=0.04) fell to 2.010 µm from 2.249 µm .which implies the Ba^{2+}addition inhibits grain boundary mobility and suppresses the grain growth [23].

This reduction can also be correlated with pinning effect of grain boundaries from the formation of oxygen vacancies [36]. The present result agrees with the average crystallite size, D, determined with the above XRD analysis, because XRD gives crystallite size whereas SEM gives grain size [37].

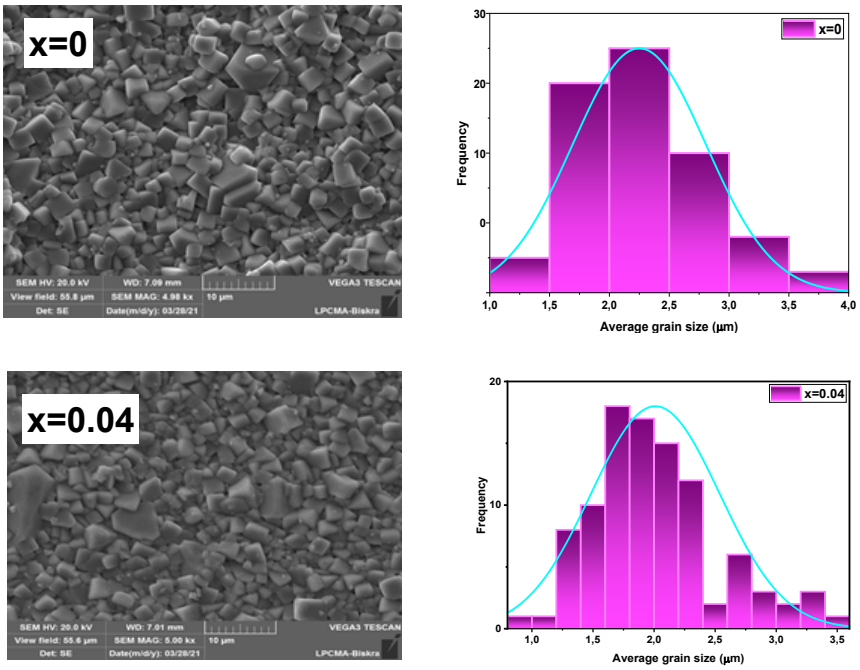

Fig.6. SEM micrograph and size distribution of the samples $NB_{1-x}B_xTZNZ$ (x=0 and x=0.04) respectively.

In addition, from the SEM micrograph of $NB_{1-x}B_xTZNZ$ (x=0.04) it can be seen that the presence of the pyrochlore phase, it is remarkable for its pyramid shape [38], and this can be shown by the following figure 7. This confirms what we found in DRX.

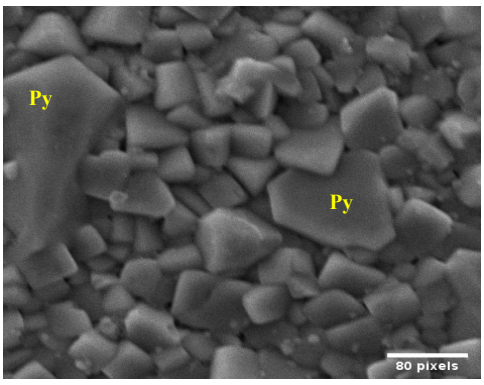

Fig. 7. High magnification image showing the shape of the pyrochlore phase in $NB_{1-x}B_xTZNZ$ (x= 0.04).

3.5. Dielectric measurements

One of the most crucial characteristics of ceramic materials is the dielectric spectrum. Therefore information about the relative permittivity of the tested material is provided by electrical research for specified orientation of the electric field and frequency depending on the types of polarizations responsible for relaxation and defects in the ceramic sample [40].

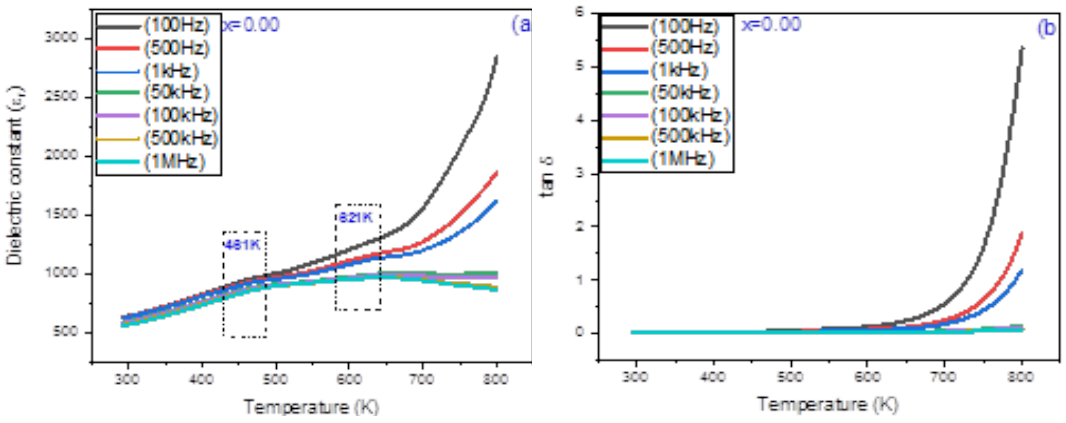

Fig.8. a)Variation of relative permittivity ε_r,, and b) tangent loss tanδ, of $NB_{1-x}B_xTZNZ(x=0)$ compound with temperature at selected frequencies.

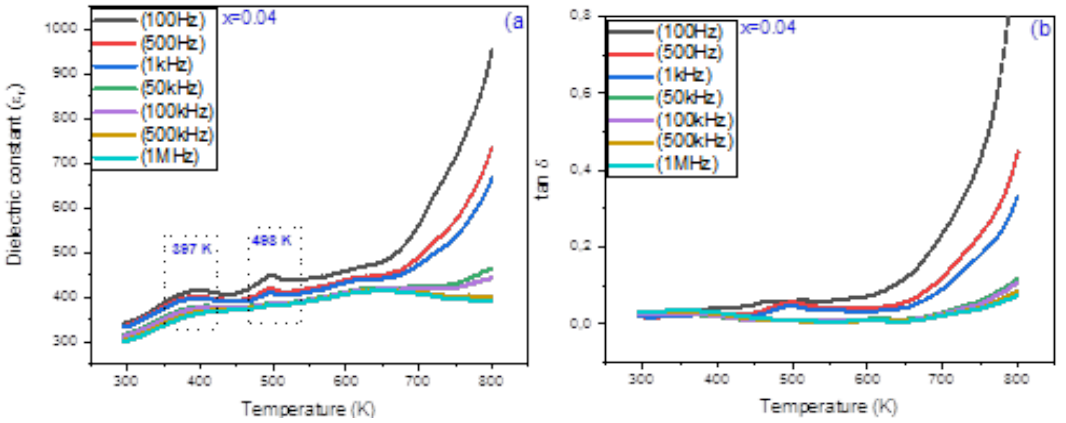

Fig. 9. a)Variation of relative permittivity ε_r,, and b) tangent loss tanδ, of $NB_{1-x}B_xTZNZ(x=0.04)$ compound with temperature at selected frequencies.

Figure (8 and 9) Show the variation of relative dielectric permittivity (ε_r) and tangent loss (tanδ) of $NB_{1-x}B_xTZNZ$ (x=0 and x=0.04) samples have a similar tendency of their variation with temperature and with frequency.

With the temperature the relative permittivity (ε_r) of each sample increases first slowly then quickly without reaching the maximum value within the temperature range of our experiment at which should have the transition between the ferroelectric phase and the paraelectric phase known in the ceramic type BNT. This rapid increase maybe due to the presence of space charge polarization in the materials [30,37,39].

The insertion of 4% of Ba^{2+} ions with the change of tolerance factor and the temperature tends to distort the perovskite lattice while changing its cell volume which indicated in table 2.

Two anomalies can be noticed on the ε_r-T curves at low frequency (≤1KHz) at T=461K and T= 621K for $NB_{1-x}B_xTZNZ$ (x=0.00) even at little less temperature T= 397K et T=498K for doped sample of 4% of Barium. These anomalies can also be distinguished in the ferroelectric region in the tanδ-T curves. It could be due to domain wall displacements at high temperature, resulting in Bi^{3+} or oxygen vacancies induced by new doping in the crystal lattice, even some disorder in grains which can produce a relaxation charge process. The values of relative dielectric permittivity and tangent loss (tanδ) of $NB_{1-x}B_xTZNZ$ (x=0.00 and x=0.04) are classified in table 3.

The change in value of relative permittivity ε_r of materials depends on grains, grains boundaries and different types of defects like oxygen and bismuth vacancies present in the material $NB_{1-x}B_xTZNZ$ (x=0.04), generally these important factors lower the value of relative

permittivity (ε_r) [40].And this decrease in the dielectric constant may be due to the difficulty of reversing the polarization of the domains in the small grains [11].

About the angle of loss (tanδ), it is clearly observed for the two samples, that this electrical dissipation factor first increases slowly with the increase in temperature until reaching a maximum value at high temperature. The highest losses of (0.02188, 0.02147 at 298K) in 100Hz and 500Hz respectively are defined in the undoped system, on the other hand, they are in order of (0.02017, 0.0188 at 298K) are lower in the doped system which has a greater density than undoped one.

This reduction in (tanδ) for $NB_{1-x}B_xTZNZ$ (x=0.04) may be due to a decrease in the electrical conductivity of the residual current and absorption current [13]. So, we will study the conductivity and the activation energy for these simples.

Table 3. comparison of values of dielectric constant (ε_r), and loss tangent (tanδ) at 298K temperature, and the activation energie E_a at different frequencies of $NB_{1-x}B_xTZNZ$ (x=0 and x= 0.04).

	x=0.00			x=0.04		
Frequency	ε_r	Tan δ	Ea	ε_r	Tan δ	Ea
100Hz	641.05	0.02188	1.219	341.54	0.02017	0.8384
500Hz	628.61	0.02147	1.0138	335.91	0.0188	0.7519
1KHz	622.85	0.02176	0.9234	333.27	0.01906	0.73509
50KHz	587.66	0.02666	0.4569	316.32	0.02457	0.7175
500KHz	564.12	0.03395	0.3574	304.18	0.03045	0.6693
1MHz	557.44	0.03811	0.2785	300.28	0.0326	0.6416

3.6. Studies of electrical conductivity

The ac conductivity of material was calculated using the well-known relation [11, 42]:

$$\sigma_{ac} = \omega \varepsilon_r' \varepsilon_0 \tan\delta \tag{10}$$

where ω: 2πf is the angular frequency, ε_r': is the relative permitivity and ε_0: is the vacuum dielectric constant.

Figure 10shows the variation of ac conductivity with inverse of absolute temperature at some selected frequencies of $NB_{1-x}B_xTZNZ$ (x=0 and x=0.04).

For all temperature the conductivity of the material increases with an increase in frequency.

In this study, the substitution of Bi^{3+}/Na^+ by Ba^{2+} at A-site decreases the grain size and leads to the formation of Oxygene vacancies and Bi^{3+} vacancies. We found that the conductivity of the undoped sample is maximum and its value reduces for the Ba^{2+} doped sample. This type of reduction can be attributed to ion compensation resulting from the formation of both oxygen vacancies and ion vacancies [41]. And maybe the decrease of grain size for the $NB_{1-x}B_xTZNZ$ (x=0.04) sample, which results in grain boundaries growththerefore less electron transfer from grain to grain [1], because in ceramic material the dielectric structure is made from two layers, the first corresponds to conductive grains and the second to poorly conductive grains boundaries [30].

The conduction mechanism was determined by analyzing the activation energies. The activation energy of the samples is calculated based on the Arrhenius relationship [30]:

$$\sigma_{ac} = \sigma_0 exp\left(\frac{-E_a}{K_b T}\right) \tag{11}$$

where:$\sigma_0$represents the pre-exponentiel factor, $K_b$represents the Boltzmann constant and T stands for the absolute temperature.

To estimate the activation energy, a graph is plotted between $\ln(\sigma_{ac})$ and$1000/T$. The slope and intercept of the plot determine the activation energy [41]. The values of activation energy are given in table 3.

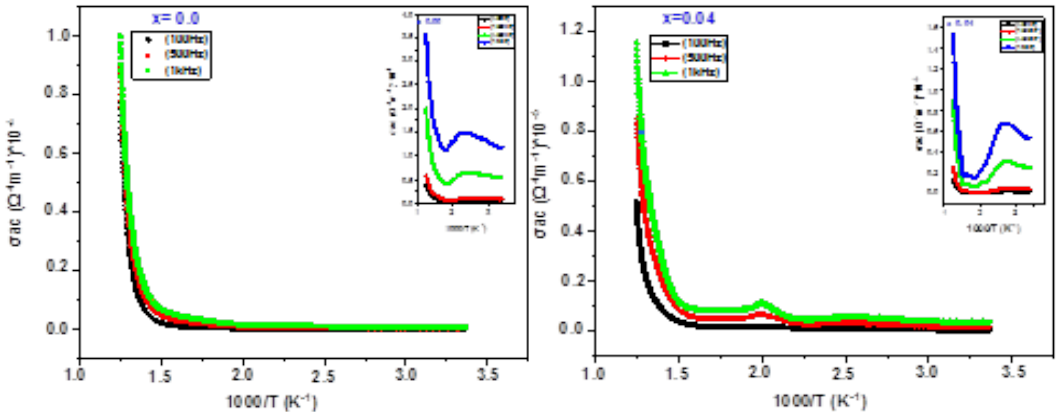

Fig. 10. Variation of ac conductivity with inverse temperature at different frequencies of $NB_{1-x}B_xTZNZ$ (x=0 and x=0.04) ceramics.

It is clear from the table 3 that in with increases in frequency the value of the activation energy decreases which may be due to the improved electronic jumps between localized states. We know that the activation energy is nothing but the minimum amount of energy required to activate atoms or molecules into a state in wich they can undergo physical transformation [30]. Also, the activation energy obtained for the Ba^{2+} doped ceramic proves to be relatively lower than activation energy obtained for the undoped sample at low frequencies (≤1KHz), which suggests that by substituting Ba^{2+}, it is easier to activate conduction electrons at low frequencies [41], but in high frequencies (≥50KHz) and high temperature, the activation energy obtained for the Ba^{2+} doped ceramic is found to relatively larger than activation energy obtained for the undoped sample that may be due to when Ba^{2+} ions dope into the A-site of $NB_{1-x}B_xTZNZ$ (x=0), it limits the volatilization of Bi/Na, consequently the activation increases [11].

4. Conclusion

The polycrystalline powders $NB_{1-x}B_xTZNZ$ (x=0 and x=0.04) ceramics are prepared using the Molten Salt synthesis (MS).We chose a sintering temperature of 1100°C to obtain dense ceramics with the ideal phase composition. We investigated the impact Ba^{2+} doping in the structural and morphological properties of these ceramics. Tetragonal structure was seen in the structural properties with the space groupe P4bm from X-ray diffraction and this was further validated by Raman spectroscopy. But a secondary phase pyrochlore is obtained. The results of DRX, SEM and RAMAN spectroscopy confirmed suitability of molten salt method MS. The crystallite size and the average grains size of $NB_{1-x}B_xTZNZ$ decrease with Ba^{2+} doping. The XRD patterns and Raman analysis indicate that the Ba^{2+} can be incorporated into $(Na_{0.5}Bi_{0.5})[(Ti_{0.8}Zr_{0.2})_{0.9}(Nb_{2/3}\ Zn_{1/3})_{0.1}]O_3$ matrix to form a new solid solution with the same tetragonal structure and different lattice parameters.

The dielectric permittivity and dielectric loss reduces with a raise in frequency and become stable at high frequency for all the ceramics. The ac conductivity is observed to decrease with Ba^{2+} doping, indicating its promising application in electronic devices.

Acknowledgements

The authors gratefully acknowledge professor Hamadi KHemakhem, Laboratory of multifunctional materials and applications, Faculty of sciences of Sfax, University of Sfax, Tunisia.

References

[1] M. jebli, D. Dhahri, Journal of molecular structure1254, 132238 (2022). http://doi.org/10.1016/j.molstruc.2021.132238
[2] P. G. Lucuta, F. L. Constantinescu. D. Barb, Journal. Am. Ceram. Soc. 68(10), 533(1985).http://doi.org/10.1111/j.1151-2916.1985.tb11519.x
[3] Z. Yu , H. Qian, Y. Liu, Y. Lyu, J. Mater. Sci. Mater Electron32, 28436 (2021). http://doi.org/10.1007/s10854-021-07223-4
[4] S. Zeroual, H. Lidjici, W. Chatta, H. Khemakhem, Ceramica 65**,**222 (2019). http://orcid.org/0000-0002-6888-3423
[5] R. Selvamani. G. Singh, V. Sathe, V,S.Tiwari, P.K. Gupta, J. Phys. Condens. Matter 23, 55901 (2011).
[6] K. Yao, C. Zhou, Q. Li , Z. Xiao, C. Yuan, J. Xu , G. Chen , G. Rao, J. Mater. Sci. Mater Electron32**,**24308 (2021).https://doi.org/10.1007/s10854-021-06899-y
[7] V. D. NGOC TRANS ,AMAN VLLAH, Journal of ELECTRONIC MATERIALS**5**(45), 2639 (2016). https://doi.org/10.1007/s11664-016-4448-y
[8]] M. Revelo-Castro, S. Gaona-Jurado , C. F. Villaquiran-Raigoza, Revista EIA, ISSN 1794-1237. 33(17), 1(2020). https://doi.org/10.24050/reia.v17i33.1356
[9] S. Manotham, P. Jaita , P. Butnoi, N. Lertcumfu, G. Rujijanagul, J. Alloys. Compou 897, 163021 (2022). https://doi.org/10.1016/j.jallcom.2021.163021
[10] L. Jin , Y. Huang , J. Pang , L. Zhang , R. Jing ,D. Guo, H. Du, X. Wei, Z. Xu , X. Lu , F. Wei , G. Liu, Ceramics International 46, 22889 (2020). https://doi.org/10.1016/j.ceramint.2020.06.062
[11] H. S. Mohanty, M. Jena , K. Jena, T. Dey, R. K. Nayak, T. Kata, P. panda, M. K. Sahu, H. Borkar, S R. Mohapatra, N. Tripathy, J . Mater. Sci: Mater Electron 33, 15232 (2022).http://doi.org/10.1007/s10854-022-08442-z
[12] B. Tilak, Journal of Material Sciences & Engineering1(1), 1(2012). https://doi.org/10.4172/2169-0022.1000108.
[13]] K. Ouahab, k. Bounab, Z. Necira, Journal of composite and Advanced materials 32, 265(2022). http://doi.org/10.18280/rcma.320601
[14] H. Hao, H. Liu,Y. Liu, M. Cao, S. Ouyang, J.Am. Ceram.Soc 90, 1659(2007). https://doi.org/10.1111/j.1551-2916.2007.01632.x
[15] A. Nesterovic, J. Vukmirovic, I. Stijepovic, M. Milanovic, B. Bajac, E. Toth, Z. Cvejic, V. V.Srdic. R. Soc, Open Sci 8, 202365(2021) . https://doi.org/10.1098/rsos.202365
[16] Ch. Rayssi, M. Jebli, J. Dhahri , M. Ben Henda, N. Alotaibi, Journal of Molecular Structure 1249, 131539(2022). http://doi.org/10.1016/j.molstruc.2021.131539
[17] S. Ahda , S. Misfadhila, P. Parikin , T. Y. S. P. Putra, Materials Science and Engeneering **176,** 012048(2017). http://doi.org/10.1088/1757-899x/176/1/012048
[18] T. Takenaka, K. Maruyama, K. Sakata, jpn. J. Appl. Phys 30, 2236 (1991). https://doi.org/10.1143/JJAP.30.2236
[19] C. Ma, X. Tan, Solid State Commun 150, 1497(2010). https://doi.org/10.1016/j.ssc.2010.06.006
[20] A. Benmakhlouf, R. Makhloufi, A. Boutarfaia, B. Messai, F. Hadji, Journal of Ovonic Research 19, 295(2023). https://doi.org/10.15251/JOR.2023.193.295
[21] A. Sakri, C. Bouremel, A. Bouterfaia. Journal of Chemical Technologie and Metallurgy57, 984(2022).
[22] S. Islam, N. Khatun, Md. Shehan Habib, S. Farid uddin fehad , N. Islam Tanvir, Md. Aftab Ali Shaikh , S. Tabassum , D. Islam , Md. Sajjad Hossain , A. siddika , Heliyon 8**,** 10529(2022). https://doi.org/10.1016/j.helyon.2022e10529
[23] Y. Huang, F. Li, H. Hao, F. Xia, H. Liu, S. Zhang. Journal of Materiomics 5, 385(2019). https://doi.org/10.1016/j.jmat.2019.03.006
[24] M. Resa Bafandeh. H. Sun. Han. J. Lee. Journal of Electroceramics (2021). https://doi.org/10.1007/s10832-021-00264-5
[25] J. S. Baek, J-Hyuk. Koh . J. Alloys and Compounds , 162811(2021). https://doi.org/10.1016/j.allcom.2021.162811

[26] T. Badapanda, S. Sahoo, P. Nayak. IOP conf. Series: Materials Science and Engigneering 178, 012032 (2017). http://doi.org/10.1088/1757-899X/178/1/012032
[27] F. Saouli , F. Z. Sriti , M. Abba, Z. Necira, H. Menasra , A. Beddari. Annales. chim. Sc. Mater 2, 221(2018). http://doi.org/103166/ACSM.42.221-231
[28] Y. huang, L. Zhang, R. Jing, Q. Hu, D. O. Alikin, V. Ya Shur, S. S. Islam, H. Du, x. Wei, G. Feng, L. Zhang, L. Jin, ceramics International47, 6298(2021). https://doi.org/10.1016/j.ceramint.2020.10.208
[29] H. Menasra, K. Bounab, Z. Necira, A. Meklid , A. Bouterfaia, International Journal of Thin Films Science and Technology9**,** 181(2020). http://dx.doi.org/10.18576/ijtfst/090308
[30] B.B Arya, M Mohanty, R N P. Choudhary. Materials Chemistry and Physics 279, 125717(2022). https://doi.org/10.1016/j.matchemphys.2022.125717.
[31] O. Turki, I. Zouari , F. Benabdellah, L. Seveyrat, S. Sassi , V,Perrin, H. Khemakhem , Applied Physics (2022) 128:1034. https://doi.org/10.1007/s00339-022-06178-5
[32] K Sambasiva Rao , B.TILAK, k.Ch. Varada Rajulu , A.Swathi , H. Workineh, Journal of Alloys and Compounds 509, 7121(2011).https://doi.org/10.1016/j.jallcom.2011.04.021
[33] M. ZHONG, Q. FENG, C. YUHAN, X. LIU, B. ZHU, L. MENG, C. ZHOU, J. XU, J. WANG, G. RAO. Journal of Advanced Ceramics 10, 1119(2021). https://doi.org/10.1007/s40145-021-0497-7
[34]] F. Li, J. Zhai , B. SHEN, X. Liu , K. Yang , Y. Zhang, P. Li, B. Liu , H. Zeng, Journal of applied physics 121, 054103(2017). https://dx.doi.org/10.1063/1.4975409
[35] S. Supriya. Journal of Solid State Chemistry308, 122940(2022). https://doi.org/10.1016/j.jssc.2022.122940
[36] S. Priya Balmuchu, S. Bora, P. Dobbidi. J Mater Sci: Mater Electron 33, 25704(2022). http://doi.org/10.1007/s10854-022-09265-8
[37] A. Shukla, N. Kumar, C. Behera. R.N.P. Choudhary. J Mater Sci:Mater Electron 27, 1209(2016).https://doi.org/10.1007/s10854-015-3877-3
[38] B. Suruhan, P. Francois, K. Fritscher, U. Schulz, Surface and Coatings Technology 182, 175(2004).https://doi.org/10.1016/j.surfcoat.2003.08.068
[39] R. Panigrahi, S. Hajra, M. De, A. Kumar, A.R. james, R.N.P. Choudhary. Solid State Sciences 92, 6(2019) . http://doi.org/10.1016/j.solidstatesciences.2019.04.002
[40] N. Kumar, A. Shukla, C. Behera, R.N.P Choudhary. J. Allyons. Coump 688, 858 (2016). http://dx.doi.org/10.1016/j.jallcom.2016.07.009
[41] G. Nag Bhargavi, T. badapanda, A. Khare, M. shahid Anwar, N. Brahme. Applied Physics A (2021) 127:528. http://doi.org/10.1007/s00339-021-04628-0.
[42]C. Sai Vandana, J. Guravamma, B. Hemalatha Rudramadevi, Materials Science and Engineering 149, 012180 (2016). https://doi.org/10.1088/1757-899X/149/1/012180